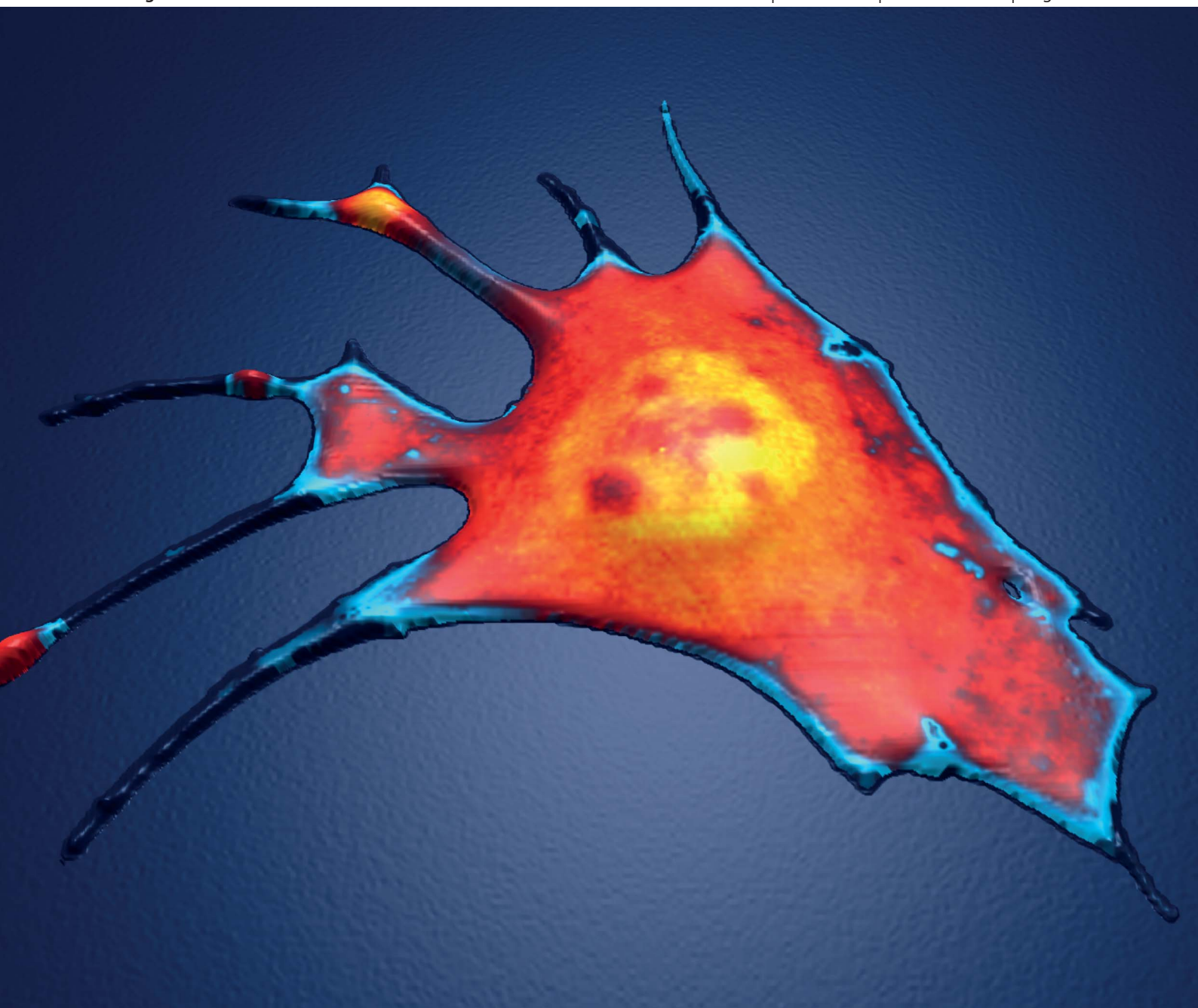


# Soft Matter

[www.rsc.org/softmatter](http://www.rsc.org/softmatter)

Volume 9 | Number 12 | 28 March 2013 | Pages 3203–3438



ISSN 1744-683X

RSC Publishing

**PAPER**

Johannes Rheinlaender and Tilman E. Schäffer  
Mapping the mechanical stiffness of live cells with the scanning ion  
conductance microscope



1744-683X(2013)9:12;1-9

# Mapping the mechanical stiffness of live cells with the scanning ion conductance microscope†‡

Cite this: *Soft Matter*, 2013, 9, 3230

Johannes Rheinlaender and Tilman E. Schäffer\*

Mapping the mechanical properties of living cells with high spatial and temporal resolution is important for the exploration of cell function. Widely used imaging techniques such as the atomic force microscope are generally based on direct mechanical contact between the probe and the cell, thereby involving the risk of damaging the cell. Here, we present a noncontact method for fast and quantitative stiffness mapping of living cells with sub-micrometer lateral resolution. This was achieved by repeatedly moving a pressurized nanopipette toward and away from the sample in a scanning ion conductance microscope (SICM). The pressure-induced microfluidic flow through the nanopipette produced a time-varying force on the sample surface, thereby locally indenting it without direct mechanical contact. Maps of sample stiffness (quantified by the Young's modulus) were then determined from ion current approach curves using a finite element model. To demonstrate the capability of the method we visualized the dynamics of individual cytoskeleton fibers in living cells over several hours. Additionally, we found that spreading extensions of migrating fibroblast cells tend to be softer than their lamellum, which is consistent with a mechanism of cell migration by osmotic swelling.

Received 18th October 2012  
Accepted 20th December 2012

DOI: 10.1039/c2sm27412d

[www.rsc.org/softmatter](http://www.rsc.org/softmatter)

## Introduction

Mechanical properties of biological materials and tissues are of great interest in the life sciences. On the level of single cells, mechanical stress has been shown to influence cell morphology, mobility, and overall molecular activity.<sup>1,2</sup> The central element of cell mechanics is the cytoskeleton. This filamentous protein network is responsible for shape, movement, and force generation.<sup>3</sup> Decoding of its properties plays a decisive role in the understanding of numerous diseases including cancer and cardiopathies.<sup>4</sup> A number of methods have been developed to probe the mechanical properties of single living cells.<sup>5</sup> Examples are optical trapping,<sup>6</sup> magnetic tweezing,<sup>7</sup> magnetic twisting cytometry,<sup>8</sup> micropipette aspiration,<sup>9</sup> or the atomic force microscopy (AFM).<sup>10</sup> Of high relevance is the ability to spatially resolve the local stiffness,<sup>11</sup> as this could give deeper insights into the structure and dynamics of the cytoskeleton, intracellular processes, and interaction between the cell and its environment.<sup>12</sup> Until now, only the AFM has allowed simultaneous topography imaging and stiffness mapping of living cells, for example in the force mapping

mode,<sup>13</sup> in the force modulation mode,<sup>14</sup> or as recently shown in the multi-harmonic tapping mode.<sup>15</sup> But these modes generally employ direct mechanical contact between the probe and the sample, thereby always involving the risk of contaminating the probe and influencing<sup>16</sup> or even damaging<sup>17</sup> the cell.

Noncontact topography images of living cells under physiological conditions can be acquired with the scanning ion conductance microscope (SICM), which uses an electrolytic current through a nanopipette as a measure for pipette–surface distance.<sup>18</sup> The noncontact character of the SICM allows for long-term measurements on living cells,<sup>19–21</sup> reliable topography imaging of soft samples,<sup>22</sup> and even unsupported lipid membranes.<sup>23</sup> Additionally, the non-contact manipulation of single cells<sup>24</sup> and even molecules has been demonstrated.<sup>25</sup>

Recently, a noncontact method for measuring the stiffness of cells using the SICM has been introduced by Sánchez *et al.*<sup>26</sup> This method is based on ramping the external pressure applied to the pipette, thereby exerting a time-varying, localized force on the sample, while a feedback loop keeps the pipette–surface distance constant. The resulting sample indentation is estimated from the change in the vertical pipette position. The stiffness is then obtained from the indentation *vs.* pressure dependency. Pellegrino *et al.*<sup>27</sup> presented an alternate approach where the sample indentation is obtained from the current–distance behavior for different values of the applied pressure. Changing the applied pressure, however, takes several seconds for each measurement location on the sample, making the acquisition of high-resolution maps on living cells impracticable.

*Institute of Applied Physics and LISA+, University of Tübingen, Auf der Morgenstelle 10, 72076 Tübingen, Germany. E-mail: [tilman.schaeffer@uni-tuebingen.de](mailto:tilman.schaeffer@uni-tuebingen.de); Fax: +49 (7071) 29-5093; Tel: +49 (7071) 29-76030*

† J.R. and T.E.S. conceived and designed the study. J.R. performed the experiments and developed the numerical model. J.R. and T.E.S. analyzed the data and wrote the manuscript.

‡ Electronic supplementary information (ESI) available. See DOI: 10.1039/c2sm27412d

Here, we present a method for measuring sample stiffness with the SICM. This method allows us to increase the measurement rate by 2–3 orders of magnitude and to simultaneously generate high-resolution, quantitative maps of sample stiffness (quantified by the Young's modulus) and topography. We resolve the dynamics of individual cytoskeleton fibers in living fibroblasts undergoing morphological changes. By correlating the stiffness with changes in topography we shed light on the interplay between mechanics and morphology in a motile cell.

## Results

### Measurement of local stiffness

For the measurement of stiffness we apply a constant pressure  $p_0$  (here: 5–10 kPa) to the upper end of the pipette (Fig. 1A). Approaching the pipette to the sample (Fig. 1B) increases the pressure on the sample, because the pressure on the sample is strongly distance dependent.<sup>26</sup> On a stiff sample the ion current rapidly decreases (Fig. 1B, left). In the case of a soft sample, the sample is progressively indented by the increasing pressure and the ion current therefore decreases more slowly (Fig. 1B, right). We recorded the ion current *vs.* the vertical pipette position (“IZ-curve”) while approaching the pipette vertically towards the sample (Fig. 1C). When a first threshold level of the ion current is reached (here: 99% of the maximum ion current  $I_0$ , here  $I_0 = 9$  nA), the vertical pipette position,  $z_0$ , is stored as a measure of sample height, similar to operation in the hopping mode.<sup>28,29</sup> When a second threshold level of the ion current is reached (here: 98% of the maximum ion current  $I_0$ ), the *z*-piezo retracts the pipette from the sample, thereby avoiding mechanical contact. Two IZ-curves recorded on a living fibroblast and on the polycarbonate substrate are shown exemplarily (Fig. 1C). For a decreasing vertical pipette position, the current initially dropped at a similar rate in both cases: the IZ-curves overlapped (Fig. 1C, region I). During further approach (Fig. 1C, region II), the current decreased faster on the stiff substrate (green trace) than it did on the soft cell (blue trace), on which it needed to approach for an additional distance  $\delta = 330$  nm to reach the second threshold level. The functional shape of an IZ-curve

therefore carries information about the local sample stiffness. To extract this information a linear regression of the IZ-curve in region II was performed either in real-time or in a subsequent off-line analysis, giving its slope  $s$ . For the two IZ-curves shown in Fig. 1C, the line fits gave  $s/I_0 = (1.99 \pm 0.07) \times 10^4 \text{ m}^{-1}$  on the cell and  $(5.54 \pm 0.40) \times 10^4 \text{ m}^{-1}$  on the substrate (the errors are estimates of the standard deviation). Alternatively, the slope could also be determined from the vertical pipette positions at the threshold levels.

### Theoretical model

To find a direct and quantitative conversion of slope  $s$  into local sample stiffness in terms of Young's modulus  $E$ , we established a model based on finite element calculations. We simulated the fluid flow, which is induced by the pressure  $p_0$  applied to the upper pipette end, and calculated the resulting deformation of an elastic sample as a function of the vertical pipette position (for details see Materials and methods). For a large vertical pipette position (Fig. 2A, top,  $z = 1.5r_i$ ), the fluid can freely diverge from the pipette opening. Thus, the pressure below the pipette is  $p \approx 0$  and nearly no force acts on the sample surface. For a decreasing vertical pipette position (Fig. 2A, middle,  $z = 0.5r_i$ ), the fluid flow is partially blocked by the sample, resulting in an increased pressure below the pipette. This pressure causes a significant sample indentation. For an even lower vertical pipette position (Fig. 2A, bottom,  $z = 0.2r_i$ ), much of the fluid flow is blocked by the sample, resulting in an even higher pressure below the pipette and an even larger sample indentation.

From a dimensional consideration it can be deduced that the deformation of the sample depends on the ratio of the Young's modulus of the sample,  $E$ , to the applied pressure,  $p_0$ . We therefore calculated IZ-curves and their slopes between 98% and 99% current for different ratios of  $E/p_0$  (Fig. 2B). We found empirically (see Materials and methods and ESI, Fig. S1†) that the relationship between the slope and the Young's modulus of the sample is well described by

$$E(s) = p_0 A \left( \frac{s}{s_\infty} - 1 \right)^{-1}, \quad (1)$$

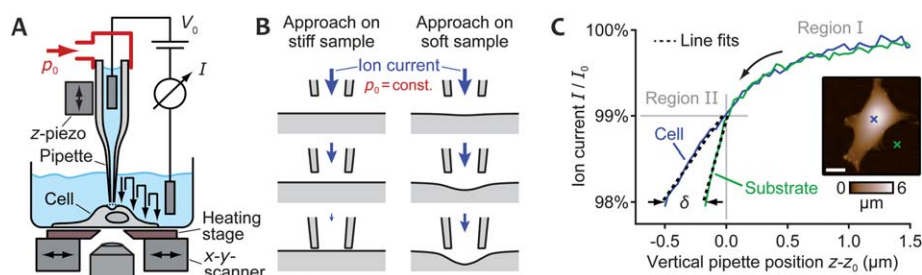


**Fig. 1** (A) Experimental setup, based on a nanopipette in proximity to a sample (here: live cell) in an electrolyte solution. A static pressure  $p_0$  (red arrow) is applied to the upper end of the pipette. The ion current through the nanopipette,  $I$ , induced by a voltage between the two electrodes,  $V_0$ , is measured. (B) Principle of the stiffness measurement. Approaching the pipette to the sample increases the pressure on the sample. A stiff sample is indented less than a soft sample. In both cases, the current decreases, but it decreases less for the soft sample (arrows). (C) Plots of ion current *vs.* vertical pipette position (“IZ-curve”) on a living fibroblast cell and on the substrate (respective positions indicated by crosses in the topography image, inset). In the initial phase of the approach, the two IZ-curves overlap (region I). The vertical pipette position at 99% current gives the undeformed sample height,  $z_0$ . Below 99% current (region II) the current drops at a smaller rate on the soft cell than it does on the stiff substrate, reflecting their different stiffnesses. The slope between 98% and 99% current is determined with a line fit. Scale bar (inset): 15  $\mu\text{m}$ .



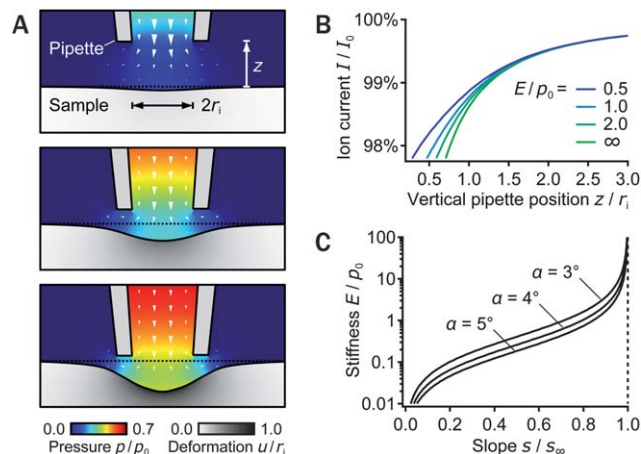


**Fig. 2** Theoretical model and quantification. (A) Quantitative simulation of fluid flow and sample deformation in the tip region. For a large vertical pipette position, the fluid can freely diverge from the pipette. Approaching the sample causes an increasing blockage of the fluid flow, a rising pressure below the pipette, and consequently an increasing sample deformation. The arrows indicate the flow velocity vector field. Modeling parameters:  $z = 1.5r_i$  (top),  $0.5r_i$  (middle), and  $0.2r_i$  (bottom); sample Young's modulus  $E = 1p_0$ ; and inner pipette half cone angle  $\alpha = 4^\circ$ . (B) Calculated IZ-curves for some values of  $E/p_0$ . (C) Calibration curves from the theoretical model to convert the measured slope of an IZ-curve between 98% and 99% current,  $s$ , into sample stiffness in terms of Young's modulus,  $E$ .  $s_\infty$  denotes the slope on an infinitely stiff sample. Curves for different values of the pipette half cone angle  $\alpha$  and a wall thickness of  $r_i/2$  are shown.

where  $s_\infty$  is the slope for an infinitely stiff sample and  $A$  is a constant depending on the pipette geometry (ESI, Table S1†). Eqn (1) is plotted for 3 different values of the pipette half cone angle  $\alpha$  (Fig. 2C). Experimentally,  $s_\infty$  is determined from IZ-curves on stiff regions of the sample (or on soft regions with no pressure applied, see also ESI, Fig. S2† for details). The threshold value pair of 99% and 98% current provided a good balance between a high signal-to-noise ratio and a low sample indentation. Furthermore, at 98% current the pipettes usually did not yet get into mechanical contact with the sample, which we routinely verified by recording IZ-curves on an AFM cantilever (ESI, Fig. S3†).

The dynamic range of the stiffness measurement can be selected by adjusting the magnitude of the applied pressure: for a softer sample a smaller pressure is used. In our setup the pressure could be varied between  $p_0 = 0.1$  and 100 kPa. In our experiments typical slopes on living cells were  $s/s_\infty \approx 0.1$ – $0.9$ , which transform into an accessible measurement range of  $E \approx 10$  Pa to 1 MPa.

The stiffness measured from an IZ-curve is subject to statistical variations due to noise of the ion current. In our experiments the relative error of the stiffness on living cells was typically on the order of a few percent (ESI, Fig. S2†).

For thin sample regions (*i.e.* indentation  $\geq 10\%$  of the sample thickness), indentation measurements overestimate the actual stiffness due to the influence of the underlying (stiff) substrate. This problem also occurs in AFM and some correction models exist,<sup>30–34</sup> but none of them is widely used yet.

## Cytoskeletal reorganization resolved with time-lapse stiffness mapping

To generate simultaneous and high-resolution maps of non-deformed sample height  $z_0(x,y)$  and stiffness  $E(x,y)$ , we recorded thousands of IZ-curves at different positions in the  $x$ - $y$  sample plane (current-volume map) using an automated script. The slope of each IZ-curve between 98% and 99% current was then determined as described above. The slope map,  $s(x,y)$ , was converted into a stiffness map,  $E(x,y)$ , using eqn (1).

We applied this method to investigate the dynamics of a live fibroblast cell adherent to a polycarbonate substrate. We imaged actin fluorescence intensity (Fig. 3, top row), cell height (Fig. 3, middle row), and cell stiffness (Fig. 3, bottom row) as functions of time. In the fluorescence images a dense network of actin fibers is present (Fig. 3A, top, small arrows) and the nucleus is clearly visible. Its perimeter is marked with a dashed white curve in the height and stiffness images, where it is not directly recognizable. The position of the nucleus coincides with the highest region of the cell (Fig. 3, middle row). While the cell topography (height) appears smooth with no substructures, the cell stiffness reveals fiber-like structures (Fig. 3A, bottom, small arrows). These fiber-like structures appear stiffer (3–10 kPa, green color) than the regions in between them (1.5–3 kPa, violet to blue color). There is a clear correlation between the fiber-like structures in the stiffness maps and the actin fibers in the fluorescence images, indicating that the contrast in the stiffness map originates from the cytoskeleton. However, not all fibers in the fluorescence images can be associated with corresponding fibers in the stiffness maps. This is owing to the fact that different cellular regions are probed by these two measurements: the contrast in the fluorescence intensity images originates from a layer around the optical focal plane at the polycarbonate substrate while the contrast in the stiffness maps originates from a layer directly below the cell surface. Additionally, regions in the fluorescence and the SICM images were acquired at different points in time as the respective image acquisition times differed.

Regions with low and high levels of active cytoskeletal reorganization can be identified in the image sequence (Fig. 3). While fluorescence, height, and stiffness in the lower left hand corner and in the right hand side of the images remained mainly unchanged, they noticeably changed in other regions (Fig. 3, large arrows). We observed both slow (Fig. 3A–D, upper large arrows) and fast (Fig. 3A–D, lower large arrow) modes of cytoskeletal reorganization.

To confirm that the contrast in the stiffness maps reflects the cytoskeleton, we added 2  $\mu$ M Cytochalasin D to the medium (between Fig. 3D and E). Cytochalasin D is a cytoskeletal drug that is known to induce the disassembly of actin fibers by blocking their plus end.<sup>35</sup> Due to continued depolymerization at their minus end this results in a net decomposition and finally in a breakdown of the actin cytoskeleton. After addition of Cytochalasin D, the fibers significantly diminished in number and finally disappeared completely in the images (Fig. 3E–G). The breakdown of the actin cytoskeleton resulted in a massive softening of the whole cell (factor of 3.9, see ESI, Fig. S4†).

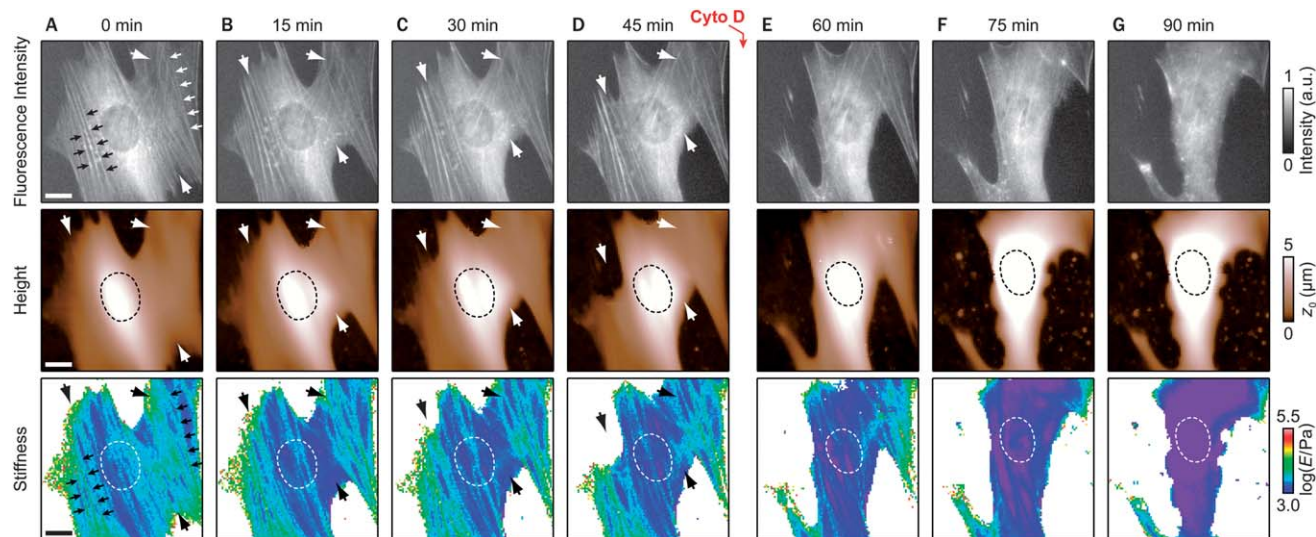


**Fig. 3** Time-lapse imaging of a live fibroblast cell revealing cytoskeleton reorganization. Seven consecutive frames of actin fluorescence (top row), SICM height (middle row), and SICM stiffness (bottom row) images are shown. (A–D) The fluorescence image shows a dense network of actin fibers. The position of the nucleus (dashed curve) coincides with the highest region of the cell (height image). The stiffness map reveals cytoskeleton fibers aligned in parallel, which can be identified as actin fibers in the fluorescence image (some marked with small arrows). Slow (upper large arrows, A–D) and fast (lower large arrow, A–D) modes of cytoskeletal reorganization processes can be seen. (E–G) After addition of 2  $\mu\text{M}$  Cytochalasin D the cytoskeleton fibers disappear in both the fluorescence image and the stiffness map, showing that the contrast in the stiffness map originates from the cytoskeleton. The fluorescence images (1 s acquisition time) were acquired immediately before the respective SICM images (15 min acquisition time, up-scan). Scale bars: 15  $\mu\text{m}$ .

A similar softening has been observed in AFM experiments.<sup>36</sup> The whole measurement sequence is shown in Movie S1 (see ESI†).

To show that our method can achieve sub-micrometer resolution in stiffness maps we imaged a living cell using a nanopipette with an inner opening radius of  $r_i \approx 100$  nm, giving a lateral resolution of 500–800 nm corresponding to 5–8 $r_i$  in this case (ESI, Fig. S5†). This is larger than the topographic lateral resolution (approximately  $3r_i$ )<sup>37</sup> by a factor of about two.

### Differential correlation analysis

As a further application we employed SICM stiffness mapping for the analysis of motility in a live fibroblast. Simultaneously recorded images of height and stiffness allowed us to correlate

morphological growth and mechanics. The height image (Fig. 4A) shows a cell with a pronounced apex in the center (large arrow) and extensions radially projecting from it (small arrows). By considering the cell's outline from the previous frame recorded 15 min before (Fig. 4A, dashed contour) it can be seen that the extensions exhibit both spreading and retraction movements with lateral velocities on the order of  $\mu\text{m}$  per min. We calculated the height change  $\Delta z_0$  between these two frames (Fig. 4B). Regions with a positive height change appear red; those with a negative change appear blue. Spreading (red) and retracting (blue) extensions are marked with small red and blue arrows, respectively. The stiffness map (Fig. 4C) reveals large variations in local cell stiffness: the cell apex (large arrow) appears softer (3–4 kPa, blue color) than the surrounding lamellum (5–10 kPa, green color). Spreading extensions

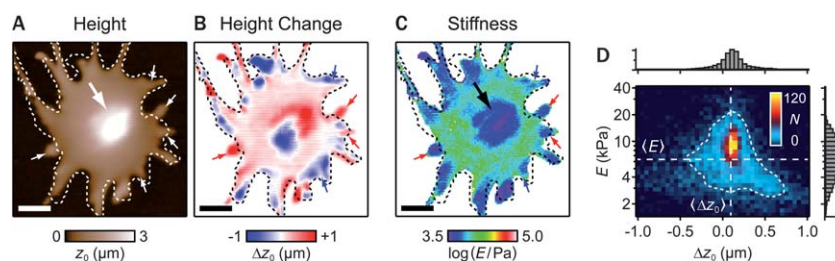


**Fig. 4** SICM topography imaging, stiffness mapping, and differential correlation analysis of a live fibroblast. (A) Height image. The cell's outline from the previous frame (15 min before) is shown as a dashed curve. (B) Height change  $\Delta z_0$  relative to the previous frame, showing spreading and retracting extensions as red and blue regions, respectively (some marked with small red and blue arrows). (C) Stiffness map, which reveals that some growing extensions (small red arrows in B and C) are significantly softer, while most of the retracting regions (small blue arrows in B and C) tend to be similar in stiffness compared to the close-by lamellum. (D) 2D histogram of stiffness and height change, and respective projections as 1D histograms. One contour level is highlighted with the closed dashed curve to guide the eye. The dashed vertical and horizontal lines indicate an average height change  $\langle \Delta z_0 \rangle = +0.1$   $\mu\text{m}$  and a log-average stiffness  $\langle E \rangle = 6.4$  kPa. The 2D distribution is skewed toward the bottom right corner, meaning that regions of increasing height are softer than the cell on an average. Scale bars: 15  $\mu\text{m}$ .

(red arrows) tend to be softer, while retracting extensions (blue arrows) tend to be similar in stiffness compared to the close-by lamellum of the same height. In order to quantify these observations, we binned the data pairs  $(\Delta z_0, E)$  into a two-dimensional histogram, where the color encodes the frequency  $N$  (Fig. 4D). The one-dimensional histograms of  $\Delta z_0$  and  $E$  are shown as projections on the top and on the right hand side, respectively. Several observations can be made: (1) the 2D distribution has a single peak at  $(\Delta z_0, E) = (0.1 \mu\text{m}, 9 \text{ kPa})$ . (2) The average height change is  $\langle \Delta z_0 \rangle = +0.1 \mu\text{m}$  (dashed vertical line) and the log-average stiffness is  $\langle E \rangle = 6.4 \text{ kPa}$  (dashed horizontal line). A positive  $\langle \Delta z_0 \rangle$  reflects an increase in cell volume, here by  $\Delta V \approx \langle \Delta z_0 \rangle \times A = +300 \mu\text{m}^3$  within 15 min (cell area  $A \approx 3000 \mu\text{m}^2$ ). (3) The 2D distribution is skewed toward the bottom right corner. We computed the linear correlation coefficient  $r$ , which is a relative measure of the degree of the correlation ( $r = +1$  would indicate a perfect positive,  $r = -1$  a perfect negative correlation), obtaining  $r = -0.21 \pm 0.05$ . A systematic analysis of 10 fibroblast cells (NIH3T3 and ATCC CRL-2645) gave correlation coefficients between  $r = -0.43$  and  $r = +0.25$ , where 70% of a total of 113 images showed a significant negative correlation. Some of the observed cells switched between positive and negative  $r$  with time. On an average, the investigated fibroblasts tended to be notably softer in regions that were rising in height. This behavior is consistent with a mechanism of cell migration by osmotic swelling, which has recently been proposed.<sup>38,39</sup>

## Conclusion

In summary, we presented a noncontact stiffness mapping method based on the SICM for quantitative, high-speed, and long-time investigation of soft samples with sub-micrometer spatial resolution. The method employs a microfluidic flow through the pipette to probe the sample with pressure-induced forces. There is no direct mechanical contact between the probe and the sample, thereby significantly reducing the risk of sample contamination or damage in comparison to other imaging techniques for the mechanical investigation of soft samples such as the AFM. Delicate samples such as live cells can thus be investigated for several hours with a high spatial and temporal resolution. Recent developments like noncontact AFM microrheology<sup>40</sup> have demonstrated the potential for a noncontact determination of sample stiffness, but they still need to be extended to two-dimensional mapping. We believe that SICM stiffness mapping will find widespread applications in soft matter science and especially in living cells, for example in studies of cytoskeleton structure and dynamics, intracellular processes, and interactions between the cell and its environment.

## Materials and methods

### Experimental setup

The experimental setup consisted of a home-built SICM head that was made compatible with a commercial AFM setup (MFP3D-BIO, Asylum Research) consisting of an  $x$ - $y$  piezo-

scanner interfaced with an inverted optical microscope (Nikon Ti-S, Nikon Corporation), as described previously.<sup>22</sup> The head was equipped with a fast piezo-actuator for vertical positioning of the pipette and a home-built linear variable differential transformer (LVDT) with sub-nanometer resolution as a position sensor. When applying a constant voltage,  $V_0$ , between the two electrodes, an ion current,  $I$ , flowed through the pipette, which was measured with a home-built current amplifier connected with a controller (Asylum Research). The controller also drove the  $z$ -piezo and the closed loop  $x$ - $y$ -scanner. A constant pressure,  $p_0$ , was applied to the upper end of the pipette *via* tubing using a water column for lower or a syringe for higher pressure. Typical pressures were  $p_0 = 5 \text{ kPa}$  (Fig. 1C and 3) and  $10 \text{ kPa}$  (Fig. 4) on living cells and up to  $100 \text{ kPa}$  on fixed cells; practical limits were about  $p_0 = 0.1$ – $100 \text{ kPa}$ . For even lower pressure, capillary tension could be used.<sup>41</sup>

High-resolution stiffness maps were generated by recording  $I$ - $z$ -curves at different positions in the  $x$ - $y$  sample plane ( $128 \times 128$  pixels). The vertical approach speed was  $30$ – $400 \text{ nm ms}^{-1}$ .

Nanopipettes were fabricated from borosilicate glass capillaries (1B100F-4, World Precision Instruments Inc.) using a  $\text{CO}_2$ -laser-based micropipette puller (P-2000, Sutter Instruments). For the pipettes used in this study the inner opening diameters were  $2r_i \approx 100$ – $1000 \text{ nm}$  (ESI, Fig. S6†). The pipettes typically had circular openings with a wall thickness of  $r_i/2$  and an inner half cone angle of  $\alpha = 4^\circ$  (obtained from electron microscopy, see ESI, insets of Fig. S3C†). For experiments on live cells, the  $x$ - $y$ -scanner was equipped with a custom-made, heated sample stage, consisting of a resistive heating wire and a PT100 sensor. Closed loop operation kept the bottom of the Petri dish at a temperature of  $37^\circ\text{C}$ .

### Numerical model

We performed finite element calculations using COMSOL Multiphysics (COMSOL AB). A model was designed in rotational symmetry consisting of a conical pipette in vicinity to a flat, elastic sample (Fig. 2A). The fluid flow was modeled using the Stokes equation, since inertial forces can be neglected due to low Reynolds numbers [see ESI, eqn (S3)†]. To avoid boundary effects while maintaining sufficient numerical precision, the fluid and sample domains were extended to  $10r_i$  in radial and vertical directions. The macroscopic neck of the pipette was included into the model analytically as previously described.<sup>37</sup> Since there is no established material model describing the non-linear and viscoelastic mechanical properties of living cells, they are usually described as linear-elastic materials.<sup>13–15,30,31,33,34</sup> The sample was therefore modeled as a linear-elastic solid with Young's Modulus  $E$ . A Poisson's ratio  $\nu = 0.5$  was assumed, in line with previous work on living cells.<sup>13</sup> The hydrodynamic timescale of the flow can be estimated as  $\tau = 1 \mu\text{s}$  [see ESI, eqn (S5)†], which is several orders of magnitude faster than the duration of an  $I$ - $z$ -curve, thereby justifying our quasi-static model.

We verified that the numerical model correctly describes the indentation of the sample by a measurement on a fixed fibroblast cell (ESI, Fig. S7A–C†). We found that the functional form



of the measured  $IZ$ -curve closely matches the curve from the numerical model, as shown on both a stiff area (substrate) and a soft area (cell) of the sample. To further validate the accuracy of the model, we also measured the local stiffness using AFM force mapping<sup>13</sup> (ESI, Fig. S7D–F†). Both methods gave identical sample stiffness. For this comparison we used fixed cells because living cells would have changed significantly while switching between AFM and SICM.

Next, we attempted to find an analytical relationship between the slope of the  $IZ$ -curve between 98% and 99% ion current and the sample stiffness. We therefore calculated  $IZ$ -curves for varying ratios of  $E/p_0$ . As shown in Fig. S1† the relationship between the slope of the  $IZ$ -curve and Young's modulus of the sample is well described by

$$\frac{s_\infty}{s} - 1 = A \left( \frac{E}{p_0} \right)^{-1} \quad (2)$$

over several orders of magnitude.  $s_\infty$  is the slope for an infinitely stiff sample and  $A$  is a parameter that depends on the pipette geometry (Table S1†). Eqn (2) can be rearranged to obtain eqn (1).

### Sample preparation

Mouse embryonic fibroblasts (MEF) from NIH3T3 (Fig. 3, S2, S3 and S6A–C†) and from ATCC CRL-2645 cell lines (Fig. 4, S6D–F and S7†) were maintained in low-glucose ( $1 \text{ g l}^{-1}$ ) Dulbecco's modified Eagle's medium (DMEM) supplemented with 10% (v/v) fetal calf serum, 2 mM L-glutamine, and 100 U ml<sup>−1</sup> penicillin–streptomycin at 5% (v/v) CO<sub>2</sub> and 37 °C. Cells were seeded on fibronectin-coated ( $50 \text{ } \mu\text{g ml}^{-1}$ ) cell culture dishes (for details see ref. 42). For actin fluorescence imaging, NIH3T3 cells were stable transfected with green fluorescence protein (GFP). 24–48 h after seeding the living cells were imaged in CO<sub>2</sub>-independent medium (Leibovitz L-15 medium with 10% fetal calf serum) at 37 °C. For the comparison with AFM (ESI, Fig. S7†), the cells were fixed 24–48 h after seeding in 4% formaldehyde for 10 min, then rinsed and imaged in phosphate-buffered saline (PBS) at room temperature.

### Fluorescence imaging

For fluorescence imaging the optical microscope was equipped with a Nikon Intensilight system. We used a 40× objective, excitation at 450–490 nm, and detection above 515 nm for GFP imaging. The images were captured using a Nikon Digital Sight DS-Vi1 CCD camera and were background and intensity corrected for maximum contrast.

### Statistical analysis

For the differential correlation analysis (Fig. 4), the (Pearson's) linear correlation coefficient  $r$  for the data pairs (height change  $\Delta z_0$  and stiffness  $E$ ) was calculated as

$$r = \frac{\text{Cov}[\Delta z_0, \log(E)]}{\sqrt{\text{Var}(\Delta z_0) \text{Var}[\log(E)]}}, \quad (3)$$

where  $\text{Cov}[\Delta z_0, \log(E)]$  is the covariance and  $\text{Var}(\Delta z_0)$  and  $\text{Var}[\log(E)]$  are the variances of  $\Delta z_0$  and  $\log(E)$ , respectively.<sup>43</sup>

The logarithm of the stiffness was used since the stiffness is log-normally distributed in living cells.<sup>44</sup> The standard error of the correlation coefficient is

$$s_r = \sqrt{\frac{1-r^2}{n-2}}, \quad (4)$$

where  $n$  is the number of data pairs.<sup>43</sup>

## Acknowledgements

We thank W. H. Goldmann and B. Fabry from the University of Erlangen-Nürnberg for providing the cell lines and for discussions, S. Kienle and A. Schönborn for assistance in cell culture, and Asylum Research for support.

## References

- 1 P. A. Janmey, *Physiol. Rev.*, 1998, **78**, 763–781.
- 2 T. D. Pollard and G. G. Borisy, *Cell*, 2003, **112**, 453–465.
- 3 A. Mogilner and K. Keren, *Curr. Biol.*, 2009, **19**, R762–R771.
- 4 J. T. Parsons, A. R. Horwitz and M. A. Schwartz, *Nat. Rev. Mol. Cell Biol.*, 2010, **11**, 633–643.
- 5 K. E. Kasza, A. C. Rowat, J. Liu, T. E. Angelini, C. P. Brangwynne, G. H. Koenderink and D. A. Weitz, *Curr. Opin. Cell Biol.*, 2007, **19**, 101–107.
- 6 A. Ashkin and J. M. Dziedzic, *Proc. Natl. Acad. Sci. U. S. A.*, 1989, **86**, 7914–7918.
- 7 A. R. Bausch, F. Ziemann, A. A. Boulbitch, K. Jacobson and E. Sackmann, *Biophys. J.*, 1998, **75**, 2038–2049.
- 8 N. Wang, J. P. Butler and D. E. Ingber, *Science*, 1993, **260**, 1124–1127.
- 9 E. A. Evans, *Biophys. J.*, 1983, **43**, 27–30.
- 10 G. Binnig, C. F. Quate and C. Gerber, *Phys. Rev. Lett.*, 1986, **56**, 930–933.
- 11 H. Huang, R. D. Kamm and R. T. Lee, *Am. J. Physiol.: Cell Physiol.*, 2004, **287**, C1–C11.
- 12 D. E. Discher, P. A. Janmey and Y. Wang, *Science*, 2005, **310**, 1139–1143.
- 13 M. Radmacher, M. Fritz, C. M. Kacher, J. P. Cleveland and P. K. Hansma, *Biophys. J.*, 1996, **70**, 556–567.
- 14 H. Haga, M. Nagayama, K. Kawabata, E. Ito, T. Ushiki and T. Sambongi, *J. Electron Microsc.*, 2000, **49**, 473–481.
- 15 A. Raman, S. Trigueros, A. Cartagena, A. P. Z. Stevenson, M. Susilo, E. Nauman and S. Antoranz Contera, *Nat. Nanotechnol.*, 2011, **6**, 809–814.
- 16 S. S. Schaus and E. R. Henderson, *Biophys. J.*, 1997, **73**, 1205–1214.
- 17 S. W. Schneider, P. Pagel, C. Rotsch, T. Danker, H. Oberleithner, M. Radmacher and A. Schwab, *Pflügers Arch. Eur. J. Physiol.*, 2000, **439**, 297–303.
- 18 P. K. Hansma, B. Drake, O. Marti, S. A. Gould and C. B. Prater, *Science*, 1989, **243**, 641–643.
- 19 Y. E. Korchev, C. L. Bashford, M. Milovanovic, I. Vodyanoy and M. J. Lab, *Biophys. J.*, 1997, **73**, 653–658.
- 20 Y. E. Korchev, J. Gorelik, M. J. Lab, E. V. Sviderskaya, C. L. Johnston, C. R. Coombes, I. Vodyanoy and C. R. Edwards, *Biophys. J.*, 2000, **78**, 451–457.

- 21 J. Gorelik, A. I. Shevchuk, G. I. Frolenkov, I. A. Diakonov, M. J. Lab, C. J. Kros, G. P. Richardson, I. Vodyanoy, C. R. Edwards, D. Klenerman and Y. E. Korchev, *Proc. Natl. Acad. Sci. U. S. A.*, 2003, **100**, 5819–5822.
- 22 J. Rheinlaender, N. A. Geisse, R. Proksch and T. E. Schäffer, *Langmuir*, 2010, **27**, 697–704.
- 23 M. Böcker, S. Muschter, E. K. Schmitt, C. Steinem and T. E. Schäffer, *Langmuir*, 2009, **25**, 3022–3028.
- 24 D. Sánchez, U. Anand, J. Gorelik, C. D. Benham, D. Bountra, M. J. Lab, D. Klenerman, R. Birch, P. Anand and Y. E. Korchev, *J. Neurosci. Methods*, 2007, **159**, 26–34.
- 25 P. Jönsson, J. McColl, R. W. Clarke, V. P. Ostanin, B. Jönsson and D. Klenerman, *Proc. Natl. Acad. Sci. U. S. A.*, 2012, **109**, 10328–10333.
- 26 D. Sánchez, N. Johnson, C. Li, P. Novak, J. Rheinlaender, Y. Zhang, U. Anand, A. Praveen, J. Gorelik, G. Frolenkov, C. Benham, M. Lab, V. Ostanin, T. E. Schäffer, D. Klenerman and Y. E. Korchev, *Biophys. J.*, 2008, **95**, 3017–3027.
- 27 M. Pellegrino, M. Pellegrini, P. Orsini, E. Tognoni, C. Ascoli, P. Baschieri and F. Dinelli, *Eur. J. Physiol.*, 2012, 1–10.
- 28 P. Happel, G. Hoffmann, S. A. Mann and I. D. Dietzel, *J. Microsc.*, 2003, **212**, 144–151.
- 29 P. Novak, C. Li, A. I. Shevchuk, R. Stepanyan, M. Caldwell, S. Hughes, T. G. Smart, J. Gorelik, V. P. Ostanin, M. J. Lab, G. W. J. Moss, G. I. Frolenkov, D. Klenerman and Y. E. Korchev, *Nat. Methods*, 2009, **6**, 279–281.
- 30 B. B. Akhremitchev and G. C. Walker, *Langmuir*, 1999, **15**, 5630–5634.
- 31 E. K. Dimitriadis, F. Horkay, J. Maresca, B. Kachar and R. S. Chadwick, *Biophys. J.*, 2002, **82**, 2798–2810.
- 32 R. Long, M. S. Hall, M. Wu and C.-Y. Hui, *Biophys. J.*, 2011, **101**, 643–650.
- 33 J. A. C. Santos, L. M. Rebelo, A. C. Araujo, E. B. Barros and J. S. de Sousa, *Soft Matter*, 2012, **8**, 4441–4448.
- 34 N. Gavara and R. S. Chadwick, *Nat. Nanotechnol.*, 2012, **7**, 733–736.
- 35 D. Bray, *Nature*, 1979, **282**, 671.
- 36 C. Rotsch and M. Radmacher, *Biophys. J.*, 2000, **78**, 520–535.
- 37 J. Rheinlaender and T. E. Schäffer, *J. Appl. Phys.*, 2009, **105**, 094905–094909.
- 38 A. Schwab, V. Nechiporuk-Zloy, A. Fabian and C. Stock, *Pflugers Arch. Eur. J. Physiol.*, 2007, **453**, 421–432.
- 39 P. Happel, K. Moller, R. Kunz and I. Dietzel, *BMC Bioinf.*, 2010, **11**, 323.
- 40 N. Gavara and R. S. Chadwick, *Nat. Methods*, 2010, **7**, 650–654.
- 41 M. Pellegrino, P. Orsini, M. Pellegrini, P. Baschieri, F. Dinelli, D. Petracchi, E. Tognoni and C. Ascoli, *Neurosci. Res.*, 2010, **69**, 234–240.
- 42 A. H. Klemm, S. Kienle, J. Rheinlaender, T. E. Schäffer and W. H. Goldmann, *Biochem. Biophys. Res. Commun.*, 2010, **393**, 694–697.
- 43 J. H. Zar, *Biostatistical analysis*, Pearson Education, Upper Saddle River, NJ, 2010.
- 44 C. Rotsch, F. Braet, E. Wisse and M. Radmacher, *Cell Biol. Int.*, 1997, **21**, 685–696.